### **ARTICLE IN PRESS**



Available online at www.sciencedirect.com

### **ScienceDirect**

Advances in Space Research xxx (xxxx) xxx

ADVANCES IN SPACE RESEARCH (a COSPAR publication)

www.elsevier.com/locate/asr

## MIOS optical subsystem for determining physical and chemical properties of meteors producing plasma irregularities

Sipeng Yang <sup>a,b,c</sup>, Zhi Wu <sup>a,b,c</sup>, Martin Dubs <sup>d</sup>, Wenjie Sun <sup>a,b,c</sup>, Lianhuan Hu <sup>a,b,c</sup>, Haiyong Xie <sup>a,b,c</sup>, Xiukuan Zhao <sup>b,c,e</sup>, Yi Li <sup>a,b,c</sup>, Baiqi Ning <sup>a,b,c</sup>, Guozhu Li <sup>a,b,c,f,\*</sup>

<sup>a</sup> Beijing National Observatory of Space Environment, Institute of Geology and Geophysics, Chinese Academy of Sciences, Beijing, China <sup>b</sup> Key Laboratory of Earth and Planetary Physics, Institute of Geology and Geophysics, Chinese Academy of Sciences, Beijing, China <sup>c</sup> Innovation Academy for Earth Science, Chinese Academy of Sciences, Beijing, China <sup>d</sup> Mirasteilas Observatory, Falera, Switzerland

<sup>e</sup> Mohe Observatory of Geophysics, Institute of Geology and Geophysics, Chinese Academy of Sciences, Beijing, China <sup>f</sup> College of Earth and Planetary Sciences, University of Chinese Academy of Sciences, Beijing, China

Received 6 August 2020; received in revised form 5 March 2021; accepted 23 March 2021

#### Abstract

A Meteor and ionospheric Irregularity Observation System (MIOS) - optical subsystem, which currently consists of 26 video cameras (4 spectrographs) at two stations Sanya (18.3°N, 109.6°E) and Ledong (18.4°N, 109°E) separated by about 70 km was developed. One of the major goals of MIOS is to study how the entry of meteoroids into the Earth's atmosphere changes the ionosphere through combining measurements of optical meteor with radar specular and non-specular meteor echoes and ionospheric irregularity echoes. This paper outlines the MIOS optical subsystem design for optical meteor detecting and methods for inferring physical and chemical properties. The spectrum and common volume optical trail observations from the two stations allow identifying emissions from meteor and atmospheric species, and calculating the meteor velocity, trajectory and orbital parameters. Preliminary results of meteors detected by the MIOS optical subsystem during July-August 2019 are presented and discussed.

© 2021 COSPAR. Published by Elsevier B.V. All rights reserved.

Keywords: Optical meteor; Meteoroid; Spectroscopy; MIOS

#### 1. Introduction

The interplanetary space is full of particles and dust (meteoroids) coming from comets and asteroids. When meteoroids enter the Earth's atmosphere due to the gravitation effect, they can create meteor light and leave plasma density enhanced trails, known as meteor trails at altitudes usually below 130 km where the air is dense enough to vaporize and ionize meteoroids' surface layers (Ceplecha

E-mail address: gzlee@mail.iggcas.ac.cn (G. Li).

https://doi.org/10.1016/j.asr.2021.03.031

0273-1177/ 2021 COSPAR. Published by Elsevier B.V. All rights reserved.

et al., 1998; Ryabova et al., 2019). The material evaporated from meteoroids can stay in the atmosphere resulting persistent layer of metallic atoms in ionospheric E region, known as the sporadic E layer, and the associated plasma trail can cause plasma instability significantly disturbing the ionosphere (e.g., Dou et al., 2010; Kelley et al., 2004; Oppenheim and Dimant, 2006).

Meteors can be detected by radio and optical instruments. The optical observations of meteors could date from 1885 when photograph was first used (Ceplecha et al., 1998). The photographic method has been widely used till the cheap low-level light video camera became available. Compared to photography, the video method

<sup>\*</sup> Corresponding author at: Key Laboratory of Earth and Planetary Physics, Institute of Geology and Geophysics, Chinese Academy of Sciences, Beijing, China.

is more sensitive with a better temporal resolution. The limiting visual magnitudes of video system, if employing EMCCD cameras, could be up to about + 10 or more (e.g., Vida et al., 2020). Many camera-based meteor observation networks have been deployed in Europe, America, Oceania and Asia, with significant contributions to the study of global meteoroid distribution, the flux of small bodies and the fall location of meteorites (e.g., Brown et al., 2002; Howie et al., 2017; Koschny et al., 2013; Madiedo, 2014).

The radio-based system is capable of full-time running regardless of the weather and suitable for estimation of total meteor activity. There are a lot of radars operated around the world for meteor specular and non-specular echo observations to derive the atmospheric parameters in the mesopause region (e.g., Holdsworth et al., 2004; Jones et al., 2005; Li et al., 2012; Oppenheim et al., 2009; Valentic et al., 1996), and the origin and evolution of interplanetary meteoroid population (Ye et al., 2016). The physical properties of meteoroids can be derived from meteor head echoes (e.g., Chau and Woodman, 2004; Janches et al., 2000; Jones et al., 2005). Although radar has the advantage of full-time running and being more sensitive for meteor detection, the chemical composition of meteoroids is hard be directly obtained from radar observation. The meteor radar usually operates at the frequency of 30– 50 MHz, i.e., with wavelength of a few meters far from the atomic emission lines ranging in nanometers. For analysis of meteoroid chemical composition, the spectrographic meteor observations have been increasingly employed (e.g., Koten et al., 2006). Simultaneous optical and radar observations of meteors were carried out to help improve the accuracy of radar detection and analysis technique (Brosch et al., 2004; Fujiwara et al., 1995; Michell and Mirizio, 2020). By employing the Southern Argentine Agile Meteor Radar (SAAMER) and optical meteor observations, Michell et al. (2015) reported that the meteor mass derived from optical system correlates well with that derived from the maximum head echo of SAAMER radar system. Li et al. (2018) conducted an observational campaign for optical meteor and radar non-specular meteor echoes at Sanya. A general linear relationship was found between the duration of non-specular echo and its corresponding meteor visual magnitude. However, some cases of optical meteors were detected within the radar field-ofview but without simultaneous radar non-specular echoes. Kelley (2004) suggested that the meteor mass and composition play an important role in the duration of meteor echoes. The analysis of meter spectra could provide important information on chemical composition, which are helpful for understanding the mechanisms controlling the meteoroid ablation process and duration of meteors (e.g., Borovicka, 1994).

To understand the physical and chemical properties of incoming meteoroids producing various meteor echo phenomena and possible processes affecting the background

ionosphere, a Meteor and ionospheric Irregularity Observation System (MIOS) is being developed to capture simultaneous optical meteor, meteor-induced plasma irregularity and ionospheric irregularity echoes. The MIOS optical subsystem, which consists of 26 video cameras (a few with diffraction gratings) deployed at Ledong (18.4°N, 109°E) and Sanya (18.3°N, 109.6°E) of Hainan Is., China, has been operated since July 2019. The MIOS radar subsystem is under construction at Ledong. The radar subsystem includes an all-sky meteor radar with operational frequency of 38.9 MHz and peak power of 20 kW, and a narrow beam radar with operational frequency of 47.5 MHz and peak power of 72 kW. The radar subsystem is sensitive to specular and non-specular meteor plasma trails, with a capability to detect meter-scale plasma irregularities within meteor trail. The all-sky meteor radar uses the typical cross array (e.g., Jones et al., 1998), with a crossed dipole antenna for transmission and five crossed dipole antennas orthogonally arranged for independent reception. The antenna array of narrow beam radar is newly designed, being composed of 15 identical modules aligned in a sword-like shape that can receive echoes separately and independently. Each module consists of  $3 \times 3$  three element Yagi antennas. Six modules are for transmission and reception, and the other modules are only for reception. The configuration of spaced antenna modules enables the radar to get the unambiguous positions of backscatter echoes through interferometry analysis. In this paper, the MIOS optical subsystem design for meteor detecting and the methods for deriving meteor physical and chemical properties are given. Some preliminary results of meteors observed during July-August 2019 are presented, including sporadic and shower meteors.

#### 2. Instrumentation

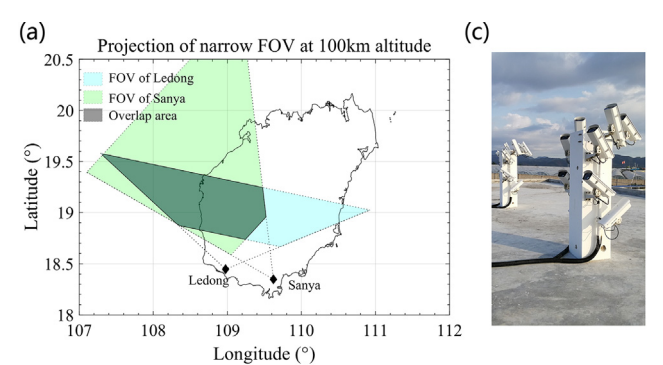
The main components of the MIOS optical subsystem include 26 low-lux CCD video cameras (Watec 902H2 Ultimate) installed at the two stations Ledong and Sanya. Out of the 26 cameras, there are 20 narrow field-of-view (FOV) cameras  $(16^{\circ} \times 12^{\circ})$  for faint meteors, 2 wide FOV cameras  $(75^{\circ} \times 60^{\circ})$  for bright meteors and 4 spectrum cameras  $(30^{\circ} \times 24^{\circ} \text{ or } 40^{\circ} \times 32^{\circ})$ . The Hikvision f/0.95 lens with focal length ranging from 7 to 33 mm is attached as narrow FOV camera, providing a limiting magnitude of about + 6.5. The Tamron f/1.2 lens with focal length 4– 12 mm is used for wide FOV camera. The FOV of MIOS optical subsystem covers  $\sim 20-80^{\circ}$  in elevation and  $\pm 70^{\circ}$ in azimuth over Ledong, and ~ 20-80° in elevation and  $-88-20^{\circ}$  in azimuth over Sanya. The average spectral resolution is about 1.2–1.8 nm/pixel. Madiedo (2017) employed both video and photographic cameras for spectral observation. The corresponding spectral resolutions are about 1.3 nm/pixel and 0.5 nm/pixel. In the work by Vojáček et al. (2015), the video cameras were equipped

with two kinds of lenses. The corresponding spectral resolutions are 3.0 nm/pixel and 1.5 nm/pixel respectively. In this study, the average spectral resolution is similar to that obtained by the video systems in Vojáček et al. (2015) and Madiedo (2017).

Fig. 1 shows the picture of outdoor cameras and the projection of FOV at 100 km altitude for the narrow and wide FOV cameras. The cameras for measuring meteor spectrum are equipped with 600 lines/mm gratings which are sensitive in the wavelength ranging between 400 and 850 nm. The video cameras generate analogue image (PAL video standard) with a rate of 25 frames per second (fps) and a resolution of 720×576 pixels. The video stream from the camera is digitized and automatically processed in near real time by the UFOCapture software for meteor detection. Only the video frames with meteor events were kept for offline analysis. Before the digitization, the GPS time inserters are employed to provide precise time for each video frame.

#### 3. Methods

To derive the physical and chemical properties of an incoming meteoroid from the recorded video, a software package was developed for observation parameters determination, meteor trail automatic recognition, meteor trajectory reconstruction, orbital elements calculation and spectrum extraction.



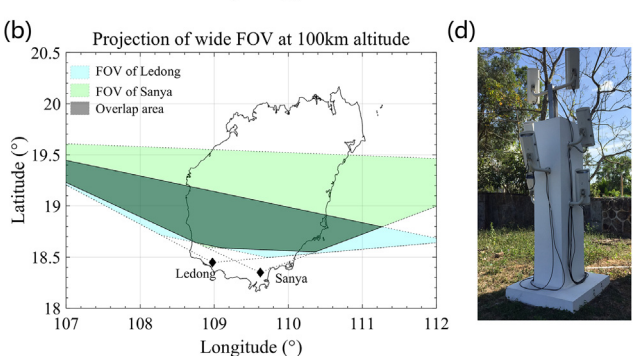


Fig. 1. (a) The equivalent FOV at 100 km altitude for all narrow FOV cameras. (b) The FOV at 100 km altitude for the two wide FOV cameras. (c, d) The pictures of outdoor cameras installed at Ledong and Sanya.

#### 3.1. Determination of observation parameters

Since the cameras were installed outdoors, the observation parameters including elevation, azimuth and rotation may be changed due to wind and other factors. These parameters are important for meteor trajectory and orbit elements calculation. It's necessary to confirm/correct the observation parameters for each meteor event. An interactive graphical user interface (GUI) was developed to obtain the accurate values of observation parameters. As shown in Fig. 2, the positions of stars obtained from the ephemeris<sup>1</sup>, marked with red crosses, were overlapped in the composite image. Through adjusting the values of observation parameters, a good coincidence between the positions of stars obtained from the observation and from the ephemeris can be achieved. The adjusted values of observation parameters are used in the analysis of corresponding meteor event.

#### 3.2. Meteor trail automatic recognition

The video data of meteor events detected by the UFOCapture were archived offline in AVI format. In each frame of the recorded video, meteor appears as a short line segment which is difficult to be automatically identified. Considering that meteor usually propagates across a few video frames, the meteor trail recognition in the offline analysis was usually performed by employing the composite image, where meteor appears as an obviously bright line. The line detection on image is usually carried out by using Hough transform (Gural, 2008). In this study, the morphological operations, dilation and erosion (Gonzales and Woods, 2002) were employed to detect the area where meteor trail was included. Then the MATLAB library function *edge* was adopted to detect the exact line.

Fig. 3 shows a case of meteor trail recognized with the edge detection method. Fig. 3a presents the original composite image where a meteor trail and a few stars can be seen. Fig. 3b shows the binarization of the composite image after employing the edge detection method, where the meteor trail is well recognized.

After recognizing a meteor trail from the composite image, the azimuth and elevation of the meteor can be obtained. The apparent visual magnitude can be estimated from the relationship between the pixel intensity and visual magnitude of stars by a linear fitting method (Weryk and Brown, 2013),

$$M = C - 2.5\log_{10}S\tag{1}$$

Where S, M and C are the sum of pixel intensity, the visual magnitude of stellar and calibration offset from least-squares fit, respectively. For the meteor event shown in Fig. 3c, the apparent visual magnitude is estimated about -0.3 by using the pixel intensity and visual magnitude of stars.

http://tdc-www.harvard.edu/catalogs/sky2k.html

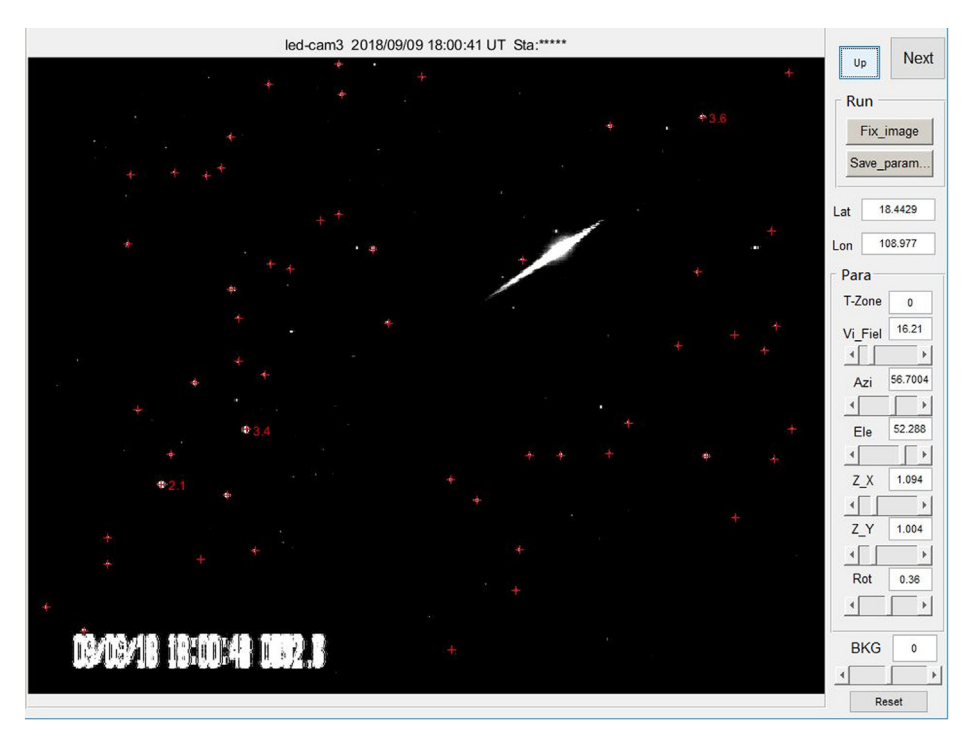


Fig. 2. The interactive graphical user interface for determining the observation parameters.

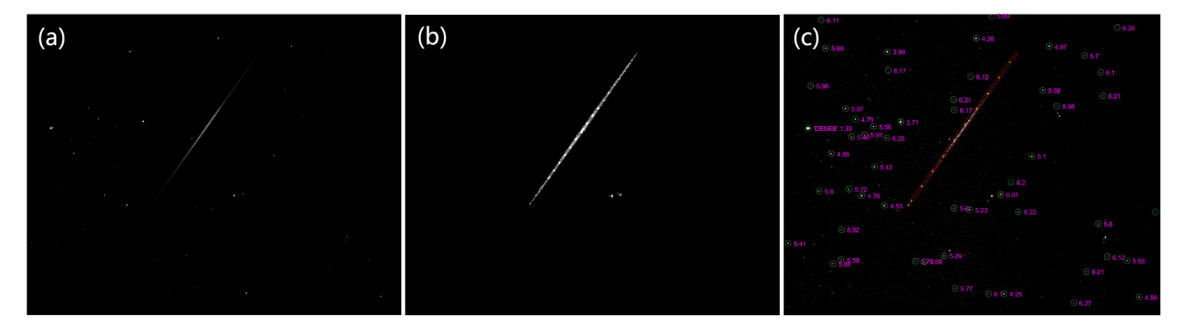


Fig. 3. (a) The original composite image with a meteor event, (b) the meteor trail recognized with the edge detection method, (c) the recognized stars and meteor trail.

## 3.3. Trajectory reconstruction and orbital elements calculation

The meteor trajectory consists of meteor radiant, beginning height and ending height. For the measurements with narrow-FOV cameras, lens distortion could be ignored so that the meteor trajectory can be regarded as a straight line. The distortion correction usually considered for a wide-angle lens (e.g., Ceplecha, 1987) was not performed for the narrow-FOV cameras of the MIOS optical subsystem. To reconstruct the trajectory of meteor detected simultaneously by the cameras at Ledong and Sanya, the plane-plane intersection method was used. In detail, the normal vector on the plane containing meteor trajectory and observation station was calculated by taking the cross product of vectors  $\mathbf{n}_1 = \mathbf{n}_{start} \times \mathbf{n}_{end}$ , where  $\mathbf{n}_{start}$  and  $\mathbf{n}_{end}$  are vectors from the station to the start and end points of a meteor trail. With the cross product of the two normal vec-

tors on two planes (for double-station observation), the directional vector of trajectory  $\mathbf{n}_{tr}$ , i.e., meteor radiant could be determined. The position of the trajectory is obtained by solving the following equation,

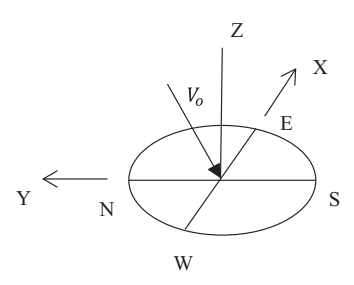


Fig. 4. A schematic diagram showing the meteor velocity vector in the topocentric horizontal coordinate system.

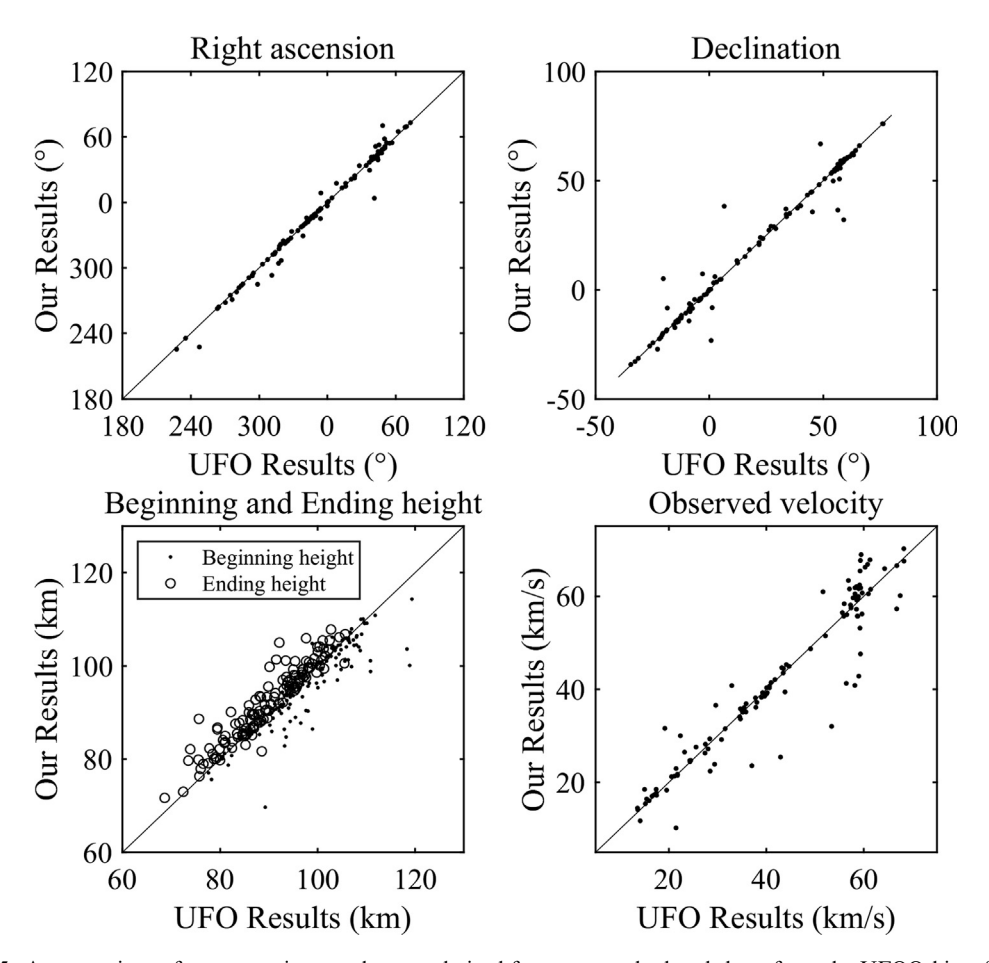


Fig. 5. A comparison of meteor trajectory elements derived from our method and those from the UFOOrbit software.

$$\begin{bmatrix} a_1 & b_1 & c_1 \\ a_2 & b_2 & c_2 \\ a_{tr} & b_{tr} & c_{tr} \end{bmatrix} \begin{bmatrix} x \\ y \\ z \end{bmatrix} = \begin{bmatrix} -d_1 \\ -d_2 \\ 0 \end{bmatrix}$$
 (2)

Where  $\mathbf{n}_1 = (a_1, b_1, c_1)$  is the normal vector on the plane containing meteor trail and one station (Ledong for the present case),  $\mathbf{n}_2 = (a_2, b_2, c_2)$  is the normal vector on the plane containing meteor trail and another station (Sanya for the present case),  $\mathbf{n}_{tr} = (a_{tr}, b_{tr}, c_{tr})$  is the directional vector of the meteor trail. The vectors are calculated in the topocentric horizontal coordinate system (Fig. 4). Once the trajectory is known, the observed velocity  $V_o$  can be obtained from the known time interval since each video frame has a GPS time stamp.

To verify the reliability of our method, we compared the results of some parameters, including the right ascension, declination, beginning and ending heights, and velocity derived from our method with those from the UFOOrbit software<sup>2</sup> using the double-station meteor data recorded in August 2019. As shown in Fig. 5, the linear consistency implies that the results from our method, in general, correspond well with those from the UFOOrbit software. Notably, for some events, there were some differences in the

parameters, for example, the velocity derived from the two methods. One possibility causing the differences is that different time stamps were used in the UFOOrbit and our software. The UFOOrbit used the time stamp saved in an XML file which was generated by the UFOCapture, a software for recording video in near real time. The UFOCapture used the Windows OS time information while recording and saving video streams. For the double station observation, there could still be a small difference between the double station OS time, whereas the OS time was periodically calibrated with GPS time. Our software used the GPS time stamp printed in each video frame image. This ensures the time consistency for double station observation and high precision of the time when each video frame was recorded. A further investigation shows that for the events with different parameter values from the two methods, their durations are very short and magnitudes are faint.

Meteoroids experience deceleration when they reach dense layers of the Earth's atmosphere. In previous studies, the atmospheric deceleration effect was not considered for fast meteors (e.g., Margonis et al., 2018). In the present analysis, the deceleration correction was not performed for all the meteor events (using  $V_o$  as the pre-atmosphere velocity  $V_\infty$ ).

<sup>&</sup>lt;sup>2</sup> http://sonotaco.com/soft/e\_index.html

With the velocity, radiant and time, the heliocentric orbital elements can be obtained by astrometric calculation and correction. The Earth's rotation and gravitational effects should be removed. The rotational velocity  $V_R$  due to the Earth's rotation depends on the latitude of station. The  $V_R$  in geocentric equatorial coordinates can be expressed as.

$$V_R(R.A.) = (2\pi(R_E(\varphi) + H_b)\cos(\varphi))/86164.091s$$

$$V_R(Dec.) = 0$$
(3b)

$$V_R(V) = 0 (3c)$$

Where  $H_b$  is the beginning altitude of meteor,  $R_E(\varphi)$  is the Earth radius at the surface projection point of the beginning point location (reference ellipsoid),  $\varphi$  is the geocentric latitude at the beginning point,  $V_R(V)$  is the component of Earth's rotational velocity in the direction of meteor.

Before a meteor is observed by ground-based camera, its speed and direction could be changed by the Earth's gravitational field. The unperturbed geocentric velocity  $V_g$  is expressed as (Porter, 1952),

$$V_{\sigma}^{2} = V^{2} - 2GM_{E}/(R_{E}(\varphi) + H_{b})$$
(4)

Where G is the gravitational constant,  $M_E$  is the Earth mass  $(GM_E = 398600.4418 \text{ km}^3/\text{s}^2)$ , V(x) is the Earth's rotation corrected velocity can be expressed as  $V(x)_{\infty} - V_R(x)$ .  $V_R(x)$  is equal to  $V_R(R.A.)$ . The relationship between the initial zenith angle  $Z_g$  and the observed zenith angle Z is described as (Porter, 1952),

$$\tan\left(\frac{1}{2}(Z_g - Z)\right) = \frac{V - V_g}{V + V_g}\tan\left(\frac{1}{2}Z\right)$$
 (5)

Based on the unperturbed velocity  $V_g$ , initial zenith angle  $Z_g$  and the azimuth  $\theta$ , the heliocentric velocity can be obtained after being transformed to heliocentric ecliptic coordinates and removing the velocity component due to the Earth's orbital motion around the Sun (Taylor, 1991).

With the meteor heliocentric position and velocity, the semi-latus rectum p was calculated according to the Kepler's law,

$$p = \frac{\left(r_m \mathbf{V}_v\right)^2}{GM_{sum}} \tag{6}$$

where  $M_{sum}$  is the mass of the sun,  $r_m$  is the distance between meteoroid and the Sun,  $v_v = \sqrt{v_x^2 + v_z^2}$  is the orbital tangential velocity.

The orbital elements including the eccentricity (e), the semi-major axis (a), the inclination (i), the longitude of the ascending node  $(\Omega)$ , and the perihelion distance (q) can then be calculated (Taylor, 1991).

To verify the developed software package for calculating meteor orbital elements, we estimated the parameters of the meteor event from Table 4 in Jenniskens et al. (2011). Table 1 shows a comparison of the results from our calculation and Jenniskens et al. In general, there is a good agreement, demonstrating that the software package works well.

Table 1 Test case. The fireball (asteroid 2008 TC<sub>3</sub>, 2:45:30.552UT, 2008 October 7) with known trajectory presented in Table 4 of Jenniskens et al. (2011), was employed to calculate the orbit elements by using our method. The Az, H and  $V_{\infty}$  are azimuth, elevation and pre-atmosphere velocity respectively.

	Jenniskens et al. (2011)	This work
Geocentric, as observed		
Az(°)	281.132	281.132
H(°)	20.736	20.736
$V_{\infty}(km/s)$	12.3823	12.3823
Geocentric, no Earth		
$R.A_g(^{\circ})$	348.2	348.1
Decl.g(°)	7.648	7.551
$V_g(km/s)$	6.349	6.324
Heliocentric		
$\lambda_h(^{\circ})$	295.150	295.192
$\beta_h(^{\circ})$	2.255	2.234
$V_h(km/s)$	32.750	32.76
Orbital elements		
q(AU)	0.909	0.910
a(AU)	1.262	1.263
e	0.280	0.280
$i(^{\circ})$	2.298	2.275
$\omega(^{\circ})$	234.202	233.827
Node(°)	194.084	193.393

#### 3.4. Spectrum extraction

The intensity profile of meteor spectrum can be derived by accumulating the gray level, i.e., the grey value indicated by the brightness of pixels, along meteor trail on the image. If the trail on an image is in a straight line, the accumulation can be done easier. This could be achieved by an image transformation method. Before the transformation, a preprocessing of image including background subtraction, flat-field correction and flat-field correction is necessary.

The background subtraction aims to remove the effects of stars, moonlight, artificial stationary lights, dark current and noise in CCD sensor. Due to the inhomogeneous gain of each pixel and the vignetting, flat-field correction is required. The preprocessing is performed for each video frame image. On the other hand, the image could have barrel distortion leading to curved light called "a hyperbola". This makes the diffraction light spreading nonlinearly in any direction at the image sensor. An image transformation method proposed by Dubs and Schlatter (2015) was applied to eliminate the hyperbola effect. By using the similar method as proposed by Rudawska et al. (2014) and Vojáček et al. (2015), the relationship between the observed wavelength and its corresponding position in pixel was determined by polynomial fitting.

According to the optic theory, the relationship between the incident light and the imaged point is gnomonic projection. After a transformation from the gnomonic to orthographic projection, the dispersion  $dx/d\lambda$  ( $\mu$ m/nm or pixel/nm) will be a constant value, fmG, over the entire image plane, where f, m, G are focal length, spectrum order and grating constant respectively. Under such condition, it will be easier to identify the spectral line with pixel dis-

tance. Spectrum calibration lamps are commonly used to determine the parameters needed for the gnomonic to orthographic projection (or  $dx/d\lambda$ ). In this work, the Hg-Ar lamp (Ocean Optics) was used. The spectrum of the lamp covers the visible light and the sensitive range of the CCD sensor. By employing the calibration lamp, the distortion parameters were obtained for image transformation.

Since the camera for meteor observation is focused at infinity, the lamp should be put away from the camera as far as possible. But it is unrealistic, considering the limited power of the lamp. Generally, the lamp and the camera are placed tens of meters away from each other in a dark room or environment. A pinhole is installed in front of the lamp and turned the light to a point source. The spectrum of the lamp would spread in the direction perpendicular to the grating line. With the known emission lines (wavelength,  $\lambda$ ) and their positions in the image (pixel number, x), we can get a set of fit parameters [ $disp_0$ ,  $c_2$ ,  $x_0$ ,  $y_0$ ] for image transformation. They are linear dispersion ( $disp_0$ ), distortion correction parameter ( $c_2$ ), the position of the optical axis ( $x_0,y_0$ ), respectively. The fitting equation is as following,

$$x = x_0 + (\lambda - \lambda_0) / disp_0 / \sqrt{\left[1 - c_2((\lambda - \lambda_0) / disp_0)\right]^2}$$
 (7)

Where  $\lambda_0$  the offset of  $\lambda$  at  $x_0$ .

Our method to obtain the fit parameters is slightly different from that described in Dubs and Schlatter (2015), as follows,

- 1. Taking several videos with lamp spectrum at different vertical offsets:
- 2. Using each spectrum taken at different offsets for fitting with the Eq. (7), and then obtaining a set of parameters  $[disp_0, c_2, x_0]$ ;
- 3. Fitting a 2th-degree polynomial to the  $disp_0$  and their offsets, then taking the y component of the extreme point (Fig. 6) of the curve as the vertical component of the optical axis, namely final $y_0$ ;

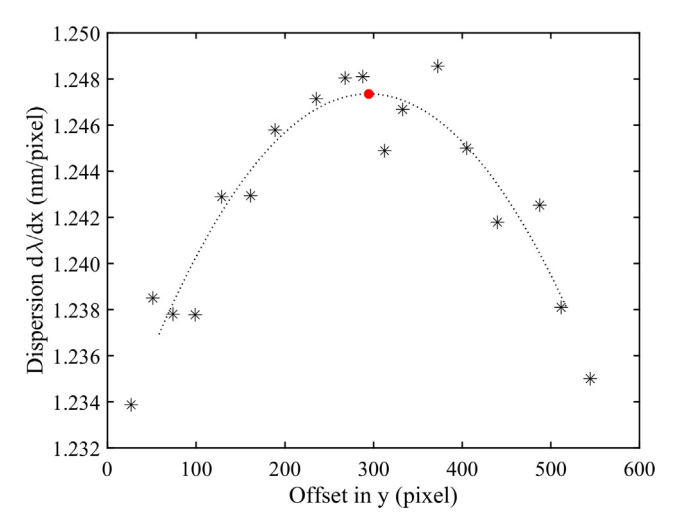


Fig. 6. Polynomial fitting to obtain the optical axis y-component position.

- 4. Finding the set of fit parameters whose  $y_0$  is closest to the final  $y_0$ , and then taking the  $disp_0$  and  $c_2$  of this set as final  $disp_0$  and  $c_2$ ;
  - 5. Taking the average of  $x_0$  from all sets as final  $x_0$ .

After these steps, the final parameters [ $disp_0$ ,  $c_2$ ,  $x_0$ ,  $y_0$ ] are obtained for image transformation.

With the final parameters  $[disp_0, c_2, x_0, y_0]$ , the composite image could be transformed, and the "hyperbola" effect could be eliminated. After the image transformation, the spectrum is extracted by adding the grey-level value of the pixels along the line. According to the zero-order or the widely used characteristic line, such as Mg-I (518.2 nm) and Na-I (589.2 nm), the other emission lines could be identified by the pixel distance and dispersion  $disp_0$ .

Fig. 7 shows a case of image transformation and wavelength scale of the Sirius spectrum. Fig. 7a and 7b show the raw composite image of Hg-Ar lamp spectra with different offsets and the transformed image, respectively. In Fig. 7b, the hyperbola effect has been eliminated. The relationship between the observed wavelength and its corresponding pixel position is linear. Fig. 7c shows a comparison of the intensity profiles of the measured Sirius spectrum and the standard stellar spectrum. Note that the measured spectrum was not sensitivity corrected, causing that the intensities of the two spectra at specific wavelengths are very different. Nevertheless, as indicated by the arrows superimposed in Fig. 7c, the absorption lines of the measured spectrum agree well with the standard spectrum, demonstrating that the wavelength scale is effective.

# 4. Preliminary results of meteors recorded by the MIOS optical subsystem

#### 4.1. Meteor properties

During July-August 2019, a total of 372 double-station meteor events and 15 spectra have been well captured and recorded. Fig. 8a shows the geographic distributions of the beginning and end heights of meteors. These meteors mainly appeared at altitudes of 70–120 km. Fig. 8b shows their radiant points. It is evident that most of the meteors were identified as sporadic, with a few meteors from the showers Perseids, Southern  $\delta$ -Aquarids and  $\alpha$ -Capricornids.

Fig. 9 shows the velocity and altitude distributions of sporadic and shower meteors. The velocities of sporadic meteors range  $\sim 11.2$ –72.8 km/s. The shower meteors have their own typical velocities. In general, larger entry velocity makes it easier to reach the ablation temperature and emit light at higher altitude where the atmosphere is thinner. The altitudes of meteors from Perseids, Southern  $\delta$ -Aquarids and  $\alpha$ -Capricornids center around 100 km, 90 km, and 90 km, respectively (Borovička and Betlem, 1997; Madiedo et al., 2014). It's worth to mention that the  $\alpha$ -Capricornids meteors have lower velocity but exhibit similar beginning height to that of the Southern  $\delta$ -Aquarids meteors. The result indicates that the physical characteris-

Advances in Space Research xxx (xxxx) xxx

S. Yang et al.

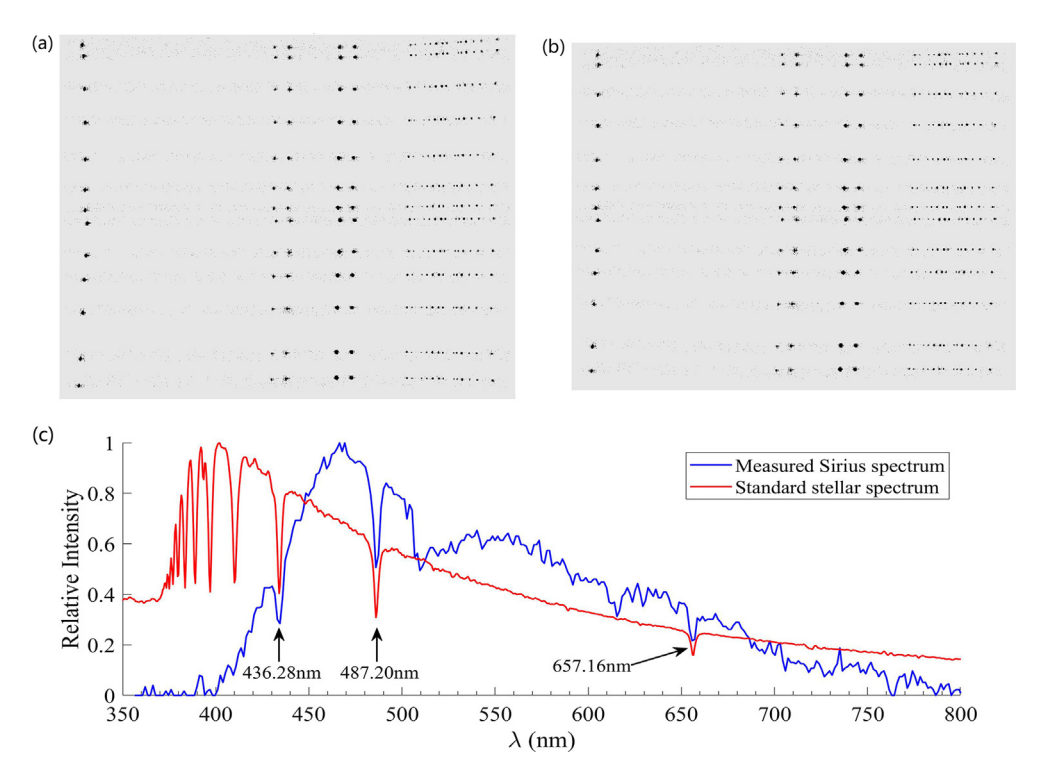


Fig. 7. (a) Raw composite image of calibration lamp spectrum recorded in different parts of the image (different offsets in y directions). (b) The transformed image of raw composite image. The hyperbola effect has been eliminated. (c) A comparison of the intensity profiles of measured Sirius spectrum and of standard stellar spectrum.

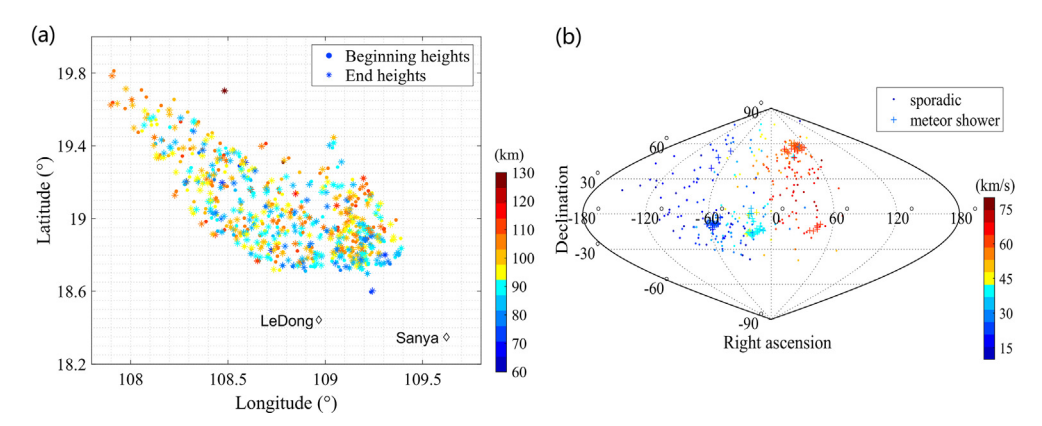


Fig. 8. (a) The geographic distributions of beginning and end heights, and (b) the radiant points of meteors detected during July-August 2019.

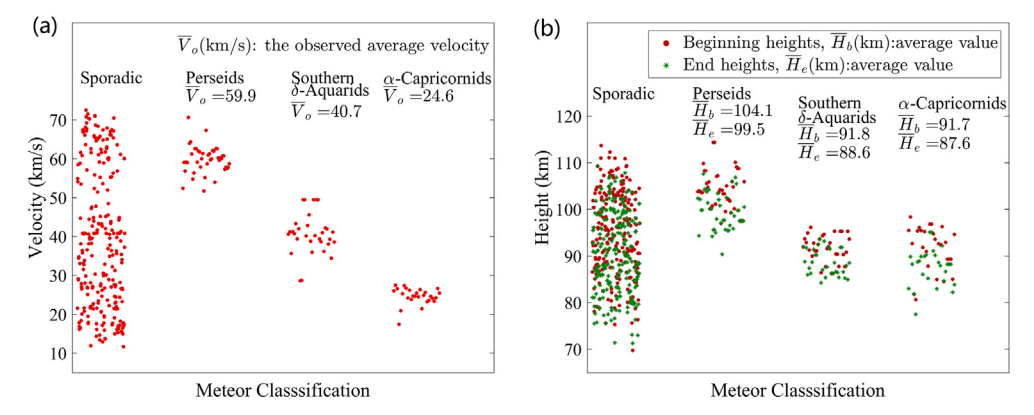


Fig. 9. (a) The entry velocities and (b) beginning and end heights of sporadic and shower meteors.

tics, such as the mass, density and structures of the meteoroids could be quite different. Previous studies suggested that  $\alpha$ -Capricornids have a lower density and higher porosity than the Southern  $\delta$ -Aquarids (e.g., Babadzhanov and Kokhirova, 2009; Narziev, 2019). The high beginning height could indicate that the material strength of parent body of  $\alpha$ -Capricornids is more fragile.

#### 4.2. Meteor chemical composition

Fig. 10 shows a case of meteor spectrum recorded by the MIOS optical subsystem. The -1 and +1 order spectra, which were captured by two cameras separately, are shown in the top and bottom panels, respectively. The intensity profiles of the spectra obtained after image transformation and accumulating along the flight path, are shown in Fig. 10b and d. The spectral resolutions are 1.3–1.4 nm/ pixel. Due to the effect of the Moon light, the signal to noise ratio of the meteor spectrum in Fig. 10a may not be so good as that in Fig. 10c. The +1 order spectrum with zero order in Fig. 10c was brighter, so its emission lines between 400 and 500 nm were clearer with higher intensity. It is evident from Fig. 10b and d that the meteor spectra are mainly emissions of atomic lines, along with other molecular and continuous radiation. A list of identified spectra lines has been given in previous works (Borovicka, 1994; Jenniskens, 2007). The present spectrum shows a common feature with main emission lines of Mg I-2 (518.2 nm), Na

I-1 (589.2 nm) and the atmospheric lines O I-1 (777.4 nm), N I-2 (821.8 nm), O I-4 (844.6 nm) and N I-2 (868.2 nm).

As the collision interaction between meteoroid and atmospheric molecules goes on, some faint emission lines appearing on the left of Mg I-2 line could be Ca I-2 (422.6 nm), Fe I-41 (438.4 nm) and Mg II-4 (448.1 nm) (please see Fig. 10c). Since the Mg II-4 (448.1 nm) is a high-temperature line, the two faint lines around 500 nm could be Fe II-42 (492.3 nm) and Fe II-42 (501.8 nm) The high-temperature line Mg II-4 respectively. (448.1 nm) suggests that this meteor could exhibit high atmosphere entry velocity. Table 2 lists the velocity, atmospheric trajectory and orbital elements of the meteor derived from the double-station observations. The uncertainties (standard deviations) were calculated using the pixels of meteor trail in the video frames within 95% prediction interval. The standard deviation of the semimajor axis a is not given here because the derived heliocentric velocity is very close to the escape velocity from the sun. Under such condition, a slight change in the derived heliocentric velocity could result in a very large variation of semi-major axis.

Fig. 11 shows the spectrum of a Perseid meteor observed at 21:44:48 on August 6, 2019. This Perseid meteor shows a quick increase in brightness early in the trail and a flare near the end. It comprises two spectral components with the temperatures of 4000 K (the neutral magnesium triplet at 516.7–518.4 nm, neutral sodium doublet at 589.0–

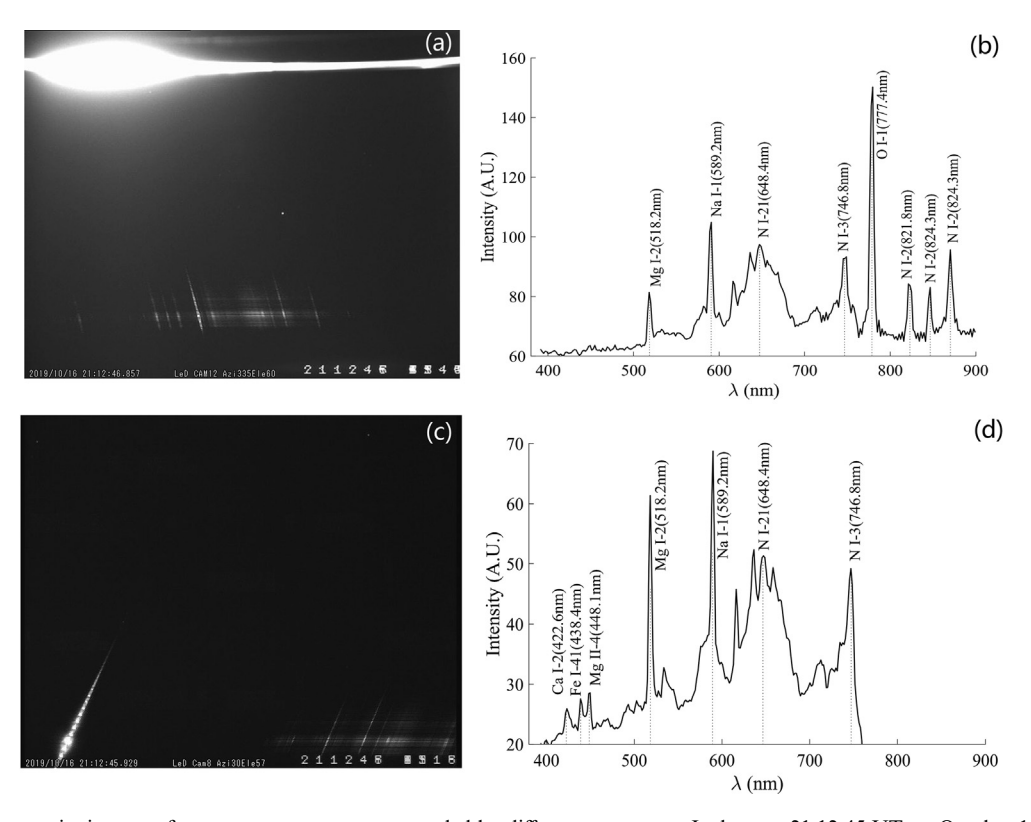


Fig. 10. (a, c) The composite images of meteor spectrum event recorded by different cameras at Ledong at 21:12:45 UT on October 16, 2019. The bright streak on the top of the composite image in the panel (a) was the Moon. (b, d) The derived spectral intensity profiles (without instrument response correction).

Table 2
The trajectory and orbital elements of meteor event recorded at 21:12:45 UT on October 16, 2019.

Meteor ID	Mag $V_g(\text{km/s})$	Ra(°)	Dec(°)	a (AU) e	i(°)	$\Omega(^{\circ})$	$\omega(^{\circ})$	q (AU)
M20191016_21124	$-4.8 \ 70.15 \pm 0.84$	$99.19 \pm 0.12$	$7.30 \pm 0.26$	$-16.77 \ 1.053 \pm 0.00$	$66 \ 151.51 \pm 0.66$	$5.22.2381 \pm 10^{-4}$	$43.65 \pm 1.24$	$0.856 \pm 0.003$

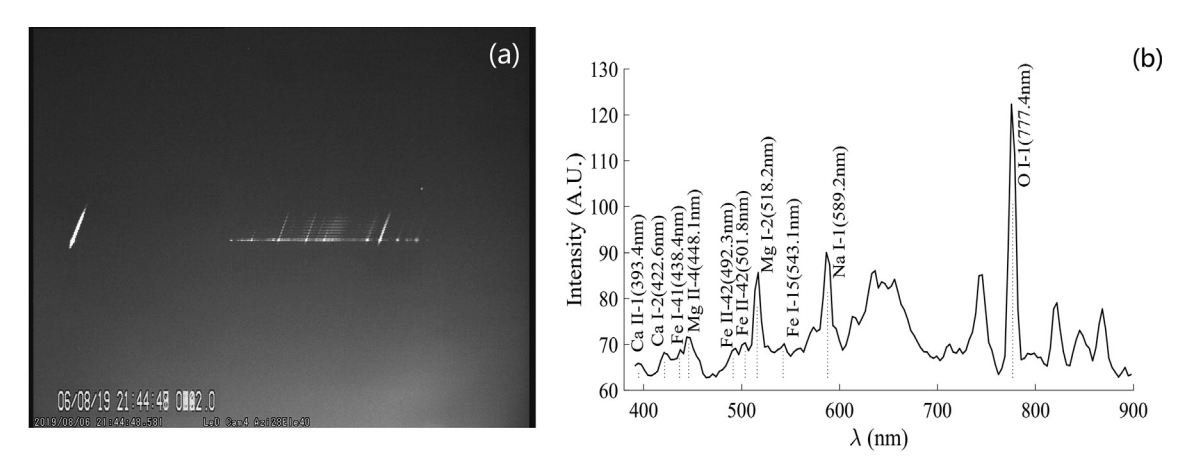


Fig. 11. (a) Case of Perseids meteor spectrum (b) and the derived raw spectral lines (without instrument response correction) observed at 21:44:48 on August 6, 2019 by the camera #4 at Ledong.

589.6 nm and neutral oxygen triplet at 777.2–777.5 nm) and 10000 K (the ionized calcium at 393.4 nm and ionized magnesium at 448.1 nm). Other atomic and ionic lines like Ca I, Fe I-41, Fe II-42, Fe I-15 were also identified. Meteor spectra could be classified according to the relative intensities of the emission lines of Mg I-2 (518.2 nm), Na I-1 (589.2 nm), and Fe I-15 multiplets at 526.9-544.9 nm (Borovička et al., 2005). The ratio values among the emission lines for shower and sporadic meteors were found to be different (Vojáček et al., 2015). For the present analysis, the system sensitivity of the video spectrograph was not corrected. The ratios cannot be derived from the intensity of raw lines. Borovicka & Betlem (1997) reported the Perseid spectra of a very bright fireball with a visual magnitude of -11. For the emission lines within 400–600 nm, the Perseid meteor spectra measured by our system are similar to those in Borovicka & Betlem, where the lowtemperature lines Ca I-2 (422.6 nm), Fe II-41 (438.4 nm), Mg I-2 (518.2 nm), Na I-1 (589.2 nm), and Fe I-15 (526.9-544.9 nm) were identified. For the emission lines detected below 400 nm by Borovicka & Betlem (1997), they were not detected by our system. The measurements by our system are cut off around 390 nm.

#### 5. Conclusions

We have described the meteor trail and spectrum detection system, as a part of the MIOS and showed some preliminary results. The main conclusions are given below:

(1) The meteor detection system hardware has been successfully set up in Sanya and Ledong observatories. A lot of meteor trails and corresponding spectra have been captured and recorded.

- (2) The data processing software has been developed. The magnitude, trajectory, velocity and preatmospheric orbit of double-station meteors were calculated using our data processing software. Outputs from our software agree well with the results derived from the UFOOrbit software. The observed  $\alpha$ -Capricornids meteors have lower velocity but exhibit similar beginning height to that of the Southern  $\delta$ -Aquarids meteors. Previous studies suggested that α-Capricornids have a lower density and higher porosity than the Southern  $\delta$ -Aquarids (e.g., Babadzhanov and Kokhirova, 2009; Narziev, 2019). The similarity between the beginning heights of  $\alpha$ -Capricornids and Southern  $\delta$ -Aquarids meteors could indicate that the material strength of parent body of  $\alpha$ -Capricornids is more fragile.
- (3) By using image transformation to scale the wavelength, the spectral intensity profile from the raw video spectrum has been obtained. An analysis of sporadic and shower meteor spectra has shown that the prominent emission lines can be identified clearly. The high-temperature line Mg II-4 (448.1 nm), which could be caused by the high atmosphere entry velocity, was identified in the sporadic meteor spectra. The Perseid meteor spectra measured by our system are similar to those in Borovicka & Betlem, where the low-temperature lines Ca I-2 (422.6 nm), Fe II-41 (438.4 nm), Mg I-2 (518.2 nm), Na I-1 (589.2 nm), and Fe I-15 (526.9–544.9 nm) were identified.

This system would provide an efficient way for the study of meteor properties. We are also expanding the MIOS optical subsystem by adding more cameras with gratings to capture meteor spectra. In future work we aim to per-

Table A1

The distortion parameters of different cameras for image transformation.

	Spectrograph#1	Spectrograph#2	Spectrograph#3	Spectrograph#4
disp <sub>0</sub> (nm/pixel)	1.8204	1.2471	1.3739	1.3470
$c_2$	6.7580e-7	4.5397e-7	4.8073e-7	4.6812e-7
$x_0(pixel)$	-1.6278	1.2018	0.5915	0.8305
$y_0(pixel)$	-6.7843	7.5323	-22.58	1.7984

form a quantitative analysis of meteor spectra to study the elemental composition of sporadic/shower meteors that will help to characterize meteoroids and their parent bodies.

#### **Declaration of Competing Interest**

The authors declare that they have no known competing financial interests or personal relationships that could have appeared to influence the work reported in this paper.

#### Acknowledgments

The MIOS is supported by the National Natural Science Foundation of China (41727803). S. Yang acknowledges the Experimental Technology Innovation Fund of the Institute of Geology and Geophysics, Chinese Academy of Sciences (E051850301). The data used in this study are archived at the Geophysics Center, National Earth System Science Data Center at BNOSE, IGGCAS (http://wdc.geophys.ac.cn/).

#### Appendix A. See Table A1

#### References

- Babadzhanov, P.B., Kokhirova, G.I., 2009. Densities and porosities of meteoroids. Astron. Astrophys. 495 (1), 353–358. https://doi.org/ 10.1051/0004-6361:200810460.
- Borovicka, J., 1994. Line identifications in a fireball spectrum. Astron. Astrophys. Suppl. Ser. 103, 83–96 http://articles.adsabs.harvard.edu/pdf/1994A%26AS.103...83B.
- Borovička, J., Betlem, H., 1997. Spectral analysis of two Perseid meteors. Planet Space Sci. 45 (5), 563–575. https://doi.org/10.1016/S0032-0633 (97)00024-X.
- Borovička, J., Koten, P., Spurný, P., Boček, J., Štork, R., 2005. A survey of meteor spectra and orbits: evidence for three populations of Na-free meteoroids. Icarus 174 (1), 15–30. https://doi.org/10.1016/j.icarus.2004.09.011.
- Brosch, N., Polishook, D., Helled, R., Schijvarg, S., Rosenkrantz, M., 2004. Radar and optical leonids. Atmos. Chem. Phys. 4, 1063–1069. https://doi.org/10.5194/acp-4-1063-2004.
- Brown, P., Spalding, R.E., Revelle, D.O., Tagliaferri, E., Worden, S.P., 2002. The flux of small near-Earth objects colliding with the Earth. Nature 420, 294–296 https://www.nature.com/articles/nature01238.
- Ceplecha, Z., 1987. Geometric, dynamic, orbital and photometric data on meteoroids from photographic fireball networks. Bull. Astron. Inst. Czech. 38 (4), 222–234 http://adsabs.harvard.edu/full/1987BAICz.38. 222C.
- Ceplecha, Z., Borovička, J., Elford, W.G., ReVelle, D.O., Hawkes, R.L., Porubčan, V., Šimek, M., 1998. Meteor phenomena and bodies. Space Sci. Rev. 84, 327–471. https://doi.org/10.1023/A:1005069928850.

- Chau, J.L., Woodman, R.F., 2004. Observations of meteor-head echoes using the Jicamarca 50MHz radar in interferometer mode. Atmos. Chem. Phys. 4, 511–521 https://hal.archives-ouvertes.fr/hal-00295413.
- Dou, X.-K., Xue, X.-H., Li, T., Chen, T.-D., Chen, C., Qiu, S.-C., 2010. Possible relations between meteors, enhanced electron density layers, and sporadic sodium layers. J. Geophys. Res-Space Phys. 115 (A6), n/a-n/a. https://doi.org/10.1029/2009JA014575.
- Dubs, M., Schlatter, P., 2015. A practical method for the analysis of meteor spectra. WGN, J. IMO 43 (4), 94–101 https://arxiv.org/abs/ 1509.07531.
- Fujiwara, Y., Ueda, M., Nakamura, T., Tsutsumi, M., 1995. Simultaneous observations of meteors with the radar and TV systems. Earth Moon Planets 68, 277–282 https://link.springer.com/content/pdf/10. 1007/BF00671516.pdf.
- Gonzales, R.C., Woods, R.E., 2002. Digital image processing, 3th ed. Prentice Hall, Cliffs, N J.
- Gural, P.S., 2008. Algorithms and Software for Meteor Detection. Earth Moon Planets 102 (1-4), 269–275. https://doi.org/10.1007/s11038-007-9161-7.
- Holdsworth, D.A., Reid, I.M., Cervera, M.A., 2004. Buckland Park allsky interferometric meteor radar. Radio Sci. 39 (5), n/a–n/a. https://doi.org/10.1029/2003RS003014.
- Howie, R.M., Paxman, J., Bland, P.A., C. Towner, M., Cupak, M., Sansom, E.K., A. R. Devillepoix, H., 2017. How to build a continental scale fireball camera network. Exp. Astron. 43 (3), 237–266. https:// doi.org/10.1007/s10686-017-9532-7.
- Janches, D., Mathews, J.D., Meisel, D.D., Zhou, Q.H., 2000. Micrometeor Observations Using the Arecibo 430 MHz Radar: I. Determination of the Ballistic Parameter from Measured Doppler Velocity and Deceleration Results. Icarus 145 (1), 53–63. https://doi.org/10.1006/icar.1999.6330.
- Jenniskens, P., 2007. Quantitative meteor spectroscopy: Elemental abundances. Adv. Space Res. 39 (4), 491–512. https://doi.org/10.1016/j.asr.2007.03.040.
- Jenniskens, P., Gural, P.S., Dynneson, L., Grigsby, B.J., Newman, K.E., Borden, M., Koop, M., Holman, D., 2011. CAMS: Cameras for Allsky Meteor Surveillance to establish minor meteor showers. Icarus 216 (1), 40–61. https://doi.org/10.1016/j.icarus.2011.08.012.
- Jones, J., Webster, A.R., Hocking, W.K., 1998. An improved interferometer design for use with meteor radars. Radio Sci. 31 (1), 55–65. https://doi.org/10.1029/97RS03050.
- Jones, J., Brown, P., Ellis, K.J., Webster, A.R., Campbell-Brown, M., Krzemenski, Z., Weryk, R.J., 2005. The Canadian Meteor Orbit Radar: system overview and preliminary results. Planet Space Sci. 53 (4), 413–421. https://doi.org/10.1016/j.pss.2004.11.002.
- Kelley, M.C., 2004. A new explanation for long-duration meteor radar echoes: Persistent charged dust trains. Radio Sci. 39 (2), 1–6. https://doi.org/10.1029/2003RS002988.
- Kelley, M.C., Swartz, W.E., Makela, J.J., 2004. Mid-latitude ionospheric fluctuation spectra due to secondary E×B instabilities. J. Atmos. Sol.-Terr. Phys. 66 (17), 1559–1565. https://doi.org/10.1016/j.jastp.2004.07.004.
- Koschny, D., Bettonvil, F., Licandro, J., Luijt, C.v.d., Mc Auliffe, J., Smit, H., Svedhem, H., de Wit, F., Witasse, O., Zender, J., 2013. A double-station meteor camera set-up in the Canary Islands CILBO. Geosci. Instrum. Method. Data Syst. 2 (2), 339–348. https://doi.org/10.5194/gi-2-339-2013.
- Koten, P., Borovicka, J., Spurný, P., Evans, S., Štork, R., Elliott, A., 2006. Double station and spectroscopic observations of the Quadrantid

- meteor shower and the implications for its parent body. Mon. Not. Roy. Astron. Soc. 366 (4), 1367–1372. https://doi.org/10.1111/j.1365-2966.2005.09913.x.
- Li, G., Ning, B., Hu, L., Chu, Y.-H., Reid, I.M., Dolman, B.K., 2012. A comparison of lower thermospheric winds derived from range spread and specular meteor trail echoes. J. Geophys. Res-Space Phys. 117 (A3), n/a-n/a. https://doi.org/10.1029/2011JA016847.
- Li, G., Ning, B., Li, A., Yang, S., Zhao, X., Zhao, B., Wan, W., 2018. First results of optical meteor and meteor trail irregularity from simultaneous Sanya radar and video observations. Earth Planet. Phys. 2 (1), 15–21 https://doi.org/10.26464/epp2018002.
- Madiedo, J.M., 2014. Robotic systems for the determination of the composition of solar system materials by means of fireball spectroscopy. Earth Planets Space 66 (1), 70. https://doi.org/10.1186/1880-5981-66-70.
- Madiedo, J.M., Trigo-Rodríguez, J.M., Ortiz, J.L., Castro-Tirado, A.J., Cabrera-Caño, J., 2014. Orbit and emission spectroscopy of α-Capricornid fireballs. Icarus 239, 273–280. https://doi.org/10.1016/j. icarus.2014.06.005.
- Madiedo, J.M., 2017. Automated systems for the analysis of meteor spectra: The SMART Project. Planet Space Sci. 143, 238–244. https:// doi.org/10.1016/j.pss.2016.12.005.
- Margonis, A., Christou, A., Oberst, J., 2018. Observations of meteors in the Earth's atmosphere: Reducing data from dedicated double-station wide-angle cameras. Astron. Astrophys. 618, A99. https://doi.org/ 10.1051/0004-6361/201832927.
- Michell, R.G., Janches, D., Samara, M., Hormaechea, J.L., Brunini, C., Bibbo, I., 2015. Simultaneous optical and radar observations of meteor head-echoes utilizing SAAMER. Planet Space Sci. 118, 95–101. https://doi.org/10.1016/j.pss.2015.04.018.
- Michell, R.G., Mirizio, E.R., 2020. The statistics of small-mass meteors observed simultaneously with optical imaging and the Poker Flat Incoherent Scatter Radar. Planet Space Sci. 190, 104994. https://doi.org/10.1016/j.pss.2020.104994.
- Narziev, M., 2019. Physical properties of the meteoroids using simultaneous radar and optical observations. Planet Space Sci. 173, 42–48. https://doi.org/10.1016/j.pss.2018.11.011.

- Oppenheim, M.M., Dimant, Y., 2006. Meteor induced ridge and trough formation and the structuring of the nighttime E-region ionosphere. Geophys. Res. Lett. 33 (24). https://doi.org/10.1029/2006gl028267.
- Oppenheim, M.M., Sugar, G., Slowey, N.O., Bass, E., Chau, J.L., Close, S., 2009. Remote sensing lower thermosphere wind profiles using non-specular meteor echoes. Geophys. Res. Lett. 36 (9). https://doi.org/10.1029/2009g1037353.
- Porter, J.G., 1952. Comets and Meteor Streams. Chapman and Hall, London, pp. 81–84.
- Rudawska, R., Zender, J., Jenniskens, P., Vaubaillon, J., Koten, P., Margonis, A., Tóth, J., McAuliffe, J., Koschny, D., 2014. Spectroscopic Observations of the 2011 Draconids Meteor Shower. Earth Moon Planets 112 (1-4), 45–57. https://doi.org/10.1007/s11038-014-9436-8.
- Ryabova, G.O., Asher, D.J., Campbell-Brown, M.D. (Eds.). 2019. Meteoroids: Sources of Meteors on Earth and Beyond (Vol. 25): Cambridge University Press.
- Taylor, A.D., 1991. A meteor orbit radar. University of Canterbury. http://hdlhandle.net/10092/8111.
- Valentic, T.A., Avery, J.P., Avery, S.K., 1996. MEDAC/SC: a third generation meteor echo detection and collection system. IEEE Trans. Geosci. Remote Sens. 34 (1), 15–21. https://doi.org/10.1109/ 36.481886.
- Vida, D., Campbell-Brown, M., Brown, P.G., Egal, A., Mazur, M.J., 2020. A new method for measuring the meteor mass index: application to the 2018 Draconid meteor shower outburst. Astron. Astrophys. 635, A153. https://doi.org/10.1051/0004-6361/201937296.
- Vojáček, V., Borovička, J., Koten, P., Spurný, P., Štork, R., 2015. Catalogue of representative meteor spectra. Astron. Astrophys. 580, A67. https://doi.org/10.1051/0004-6361/201425047.
- Weryk, R.J., Brown, P.G., 2013. Simultaneous radar and video meteors—II: Photometry and ionisation. Planet Space Sci. 81, 32–47. https://doi.org/10.1016/j.pss.2013.03.012.
- Ye, Quan-Zhi, Brown, Peter G., Pokorný, Petr, 2016. Dormant comets among the near-Earth object population: a meteor-based survey. Mon. Not. Roy. Astron. Soc. 462 (4), 3511–3527. https://doi.org/10.1093/ mnras/stw1846.